ACS Photonics

Article

Cite This: ACS Photonics 2017, 4, 2410-2418

pubs.acs.org/journal/apchd5

Spatiotemporal Dynamics and Control of Strong Coupling in Plasmonic Nanocavities

Angela Demetriadou,*[,†] Joachim M. Hamm,[†] Yu Luo,[‡] John B. Pendry,[†] Jeremy J. Baumberg,[§] and Ortwin Hess*[,†]

[†]Blackett Laboratory, Imperial College London, London, SW7 2AZ, United Kingdom

[‡]School of Electrical & Electronic Engineering, College of Engineering, Nanyang Technological University, 639798 Singapore

[§]NanoPhotonics Centre, Cavendish Laboratory, University of Cambridge, Cambridge, CB3 0HE, United Kingdom

S *Supporting Information*

ABSTRACT: In the light−matter strong coupling regime, the excited state of quantum emitters is inextricably linked to a photonic mode, leading to hybrid states that are part light and part matter. Recently, there has been a huge effort to realize strong coupling with nanoplasmonics, since it provides a versatile environment to study and control molecules in ambient conditions. Among the most promising designs are plasmonic nanocavities that confine light to unprecedentedly small volumes. Such nanocavities, though, support multiple types of modes, with different field profiles and radiative decay rates (bright and dark modes). Here, we show theoretically that the different nature of these modes leads to mode beating within the nanocavity and the Rabi oscillations, which alters the spatiotemporal dynamics of the hybrid system. By specifically designing the illumination setup, we decompose and control the dark and bright plasmon mode excitation and therefore their coupling with quantum emitters. Hence, this work opens new routes for dynamically dressing emitters, to tailor their hybrid states with external radiation.

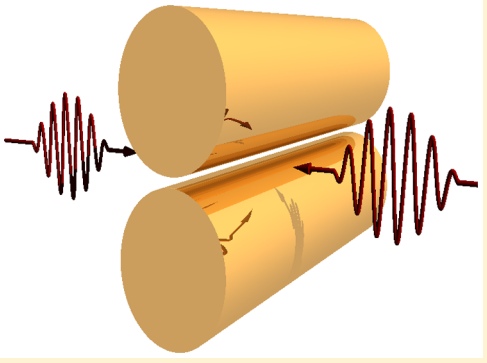

KEYWORDS: *strong coupling, nanoplasmonics, plasmonic nanocavities, dark modes, spatiotemporal dynamics, parity symmetry*

Nanophotonics and nanoplasmonics devices have the unique ability to confine light in extremely subwavelength volumes and massively enhance electromagnetic fields.[1] Based on this principle, exciting applications have emerged such as plasmonic nanoantennas,[2] colorimetric sensing,[3−5] single-molecule surface-enhanced Raman scattering,[6] and plasmonic nanocavity lasers.[7] Fundamentally, the high-field enhancement can alter the local density of states to an unprecedented degree and control the energy exchange of quantum emitters (QEs) with light.[2,8,9] For high enough field enhancement, one enters the *strong coupling regime*, where the energy exchange between QEs and plasmons is faster than the decoherence processes of the system. As a result, the excitonic state of QEs blends with the photonic mode, forming hybrid excitonic−photonic states. These hybrid states are part light, part matter and allow for the characteristic Rabi oscillations of the atomic excitations to be observed. Due to the small value of a molecule's dipole moment, strong coupling was initially realized in optical high-finesse cavities, first with many atoms[10−12] and shortly afterward for a single atom.[13] Strong coupling, where Rabi splitting is observable, generally requires atoms to be in vacuum and/or at cryogenic temperatures, where decoherence processes are suppressed.[14−17] However, plasmonic nanostructures have the ability to confine and enhance light even further (i.e., at the nanoscale)[18−21] and therefore provide an alternative route to strong coupling at room temperature. This was first demonstrated for plasmonic lattices[22−24] and J-aggregates strongly coupled to the plasmons of a single nanoparticle at ambient conditions[25,26] and recently for a single molecule strongly coupled to the plasmons in a nanocavity at room temperature.[27,28] The latter was possible only due to recent advances in self-assembled nanofabrication techniques that allow for plasmonic nanocavities with robust gaps as small as 0.34−2 nm to be fabricated.[27,29−31] By harnessing the extreme field enhancement and confinement characteristic of such plasmonic nanocavities, we can control matter at the molecular level and therefore obtain the elementary building blocks for quantum information systems,[32] controlled photochemistry at the atomic level, and manipulating chemical bonds.[33]

In this article, we demonstrate that a homogeneous layer of QEs placed in such extreme plasmonic nanocavities is strongly coupled simultaneously to multiple types of modes, resulting in complex Rabi dynamics of the hybrid system. Plasmonic nanocavities support multiple modes that depend on the parity symmetry of the nanostructure and can be spectrally degenerate, bright, or dark. Although external radiation couples dominantly to bright modes,[34] using a transformation optics

Received: May 2, 2017
Published: September 2, 2017

DOI: 10.1021/acsphotonics.7b00437
ACS Photonics 2017, 4, 2410−2418

analytical model and numerical calculations we show that in extreme plasmonic nanocavities with gaps of just a few nanometers, dark modes, which are commonly neglected[2,34] are also excited and actually contribute significantly to the field enhancement. Therefore, QEs placed in plasmonic nanocavities simultaneously exchange energy with both bright and dark plasmons, and we show that they exhibit distinctively different spatiotemporal and coupling dynamics. Here, we consider a homogeneous layer of QEs placed in a plasmonic nanocavity, and using two semiclassical descriptions (analytical and numerical), we calculate the spatiotemporal dynamics of the QE layer strongly coupled with multiple plasmon modes and demonstrate that they have identical coupling strengths, regardless of their intrinsic field enhancement, bright/dark nature, or the induced spatiotemporal asymmetries on the Rabi oscillations. The article is structured as follows: we first characterize the excited plasmons and their corresponding spatiotemporal behavior, using a transformation optics analytical model and numerical calculations, respectively. We then demonstrate that selective excitation of these modes can be achieved using double-sided illumination, and using semiclassical calculations we show both the Rabi oscillations and effective coupling strength of each mode with the QE layer. Finally, we discuss our findings for nanocavities with other parity symmetries, which exhibit different bright and dark modes.

RESULTS

By placing two metal nanowires close to each other, a plasmonic nanocavity is formed that provides high enough field enhancement to reach the strong coupling regime. In this article, we consider gold nanowires of diameter 60 nm forming a gap of 1 nm in an aqueous environment (n = 1.33), Figure 1a. A plane wave excitation propagating toward the $-x$-axis and with E_y polarization induces collective charge oscillations (plasmons) in both nanoparticles, resulting in large field enhancements and light confinement within the small gap. When no QEs are present (passive system), the absorption cross-section (Figure 1b, red full line) shows two resonances, the dipole (n = 1) mode at 620 nm and the quadrupole (n = 2) mode at 520 nm, with their respective field profiles shown in Figure 1c. Note that the quadrupole mode is at the gold interband transition frequency, which is already reflected in the permittivity of gold and actually dampens the quadrupole mode. Both the dipole and quadrupole modes have bright characteristics, and external radiation efficiently couples to both. While the quadrupole mode of an isolated nanowire is dark, for two tightly coupled nanowires the intrinsic nanoparticle modes hybridize, changing the radiative nature of the quadrupole and higher-order modes.[35−37] Using finite-difference time-domain (FDTD) methods, we excite the passive plasmonic system with a broadband pulse of 14 fs and record the spatiotemporal evolution of the E_y-field through the center of the nanocavity (Figure 1e). The broadband pulse simultaneously excites both the dipole and quadrupole modes, indicated in Figure 1e with a white and two black arrows, respectively. The central lobe of the quadrupole mode has opposite phase to the dipole mode, but is smaller in intensity. Hence, only the peripheral (side) antinodes of the quadrupole mode are visible on the spatiotemporal map, which oscillate with a higher frequency, leading

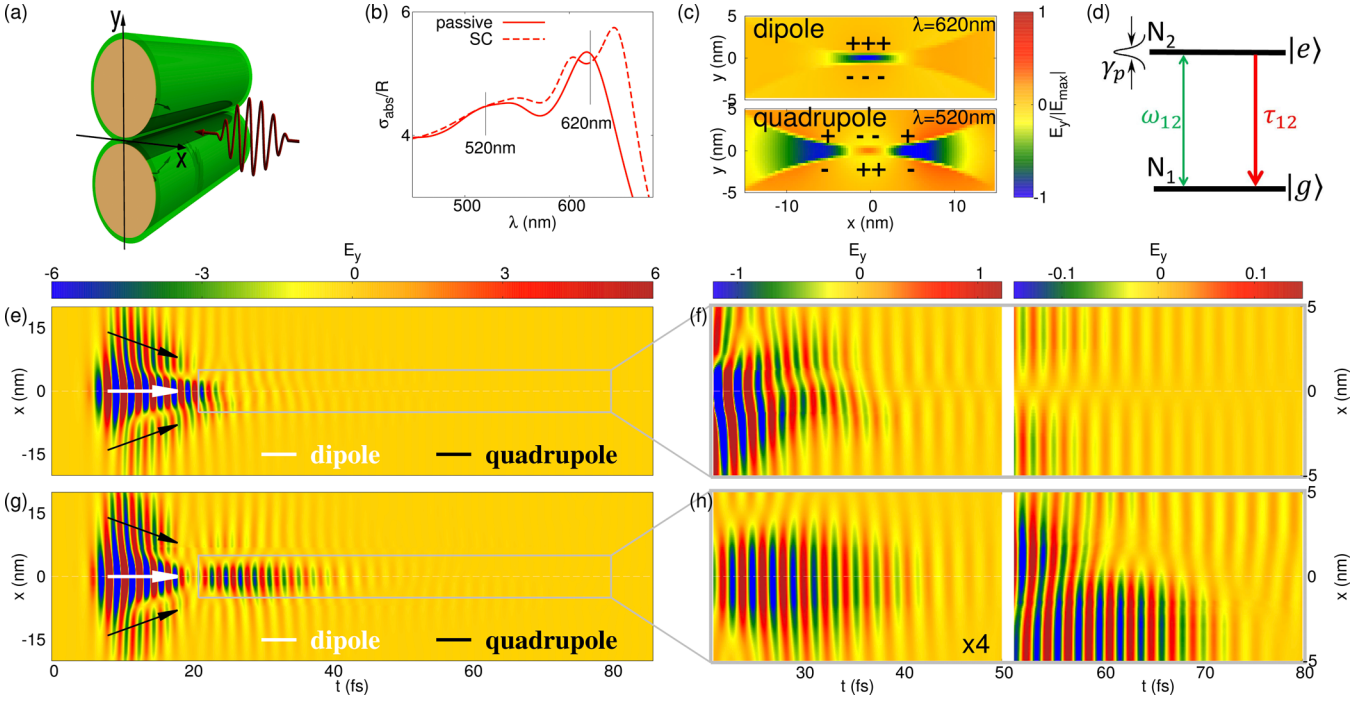

Figure 1. (a) Nanowire gold dimer structure with single pulsed source excitation and a homogeneous layer of QEs shown in green. (b) The absorption cross-section of the passive (i.e., no QEs) and the strongly coupled (i.e., with QEs) system plotted with a solid and dashed line, respectively. (c) Field profile of the dipole and quadrupole modes. (d) Representation of the two-level QEs with $\omega_{12} = 3.033 \times 10^{15}$ (rad/s) $\approx$ 2 eV $\Rightarrow$ $\lambda_{12} \approx$ 621 nm, $\tau_{12} = 10^{-9}$ s, $\gamma_p = 6.457 \times 10^{13}$ Hz, and dipole moment $\mu = 4.11 \times 10^{11} e$ m (e = elementary electronic charge). (e) Spatiotemporal map of the passive and (g) strongly coupled system, with the time evolution of the dipole and quadrupole modes shown with white and black arrows, respectively. (f) Enlarged spatiotemporal map of the passive system, where the mode beating is observed and (h) for the strongly coupled system showing the spatial asymmetry and mode beating of the Rabi oscillation.

DOI: 10.1021/acsphotonics.7b00437
ACS Photonics 2017, 4, 2410−2418

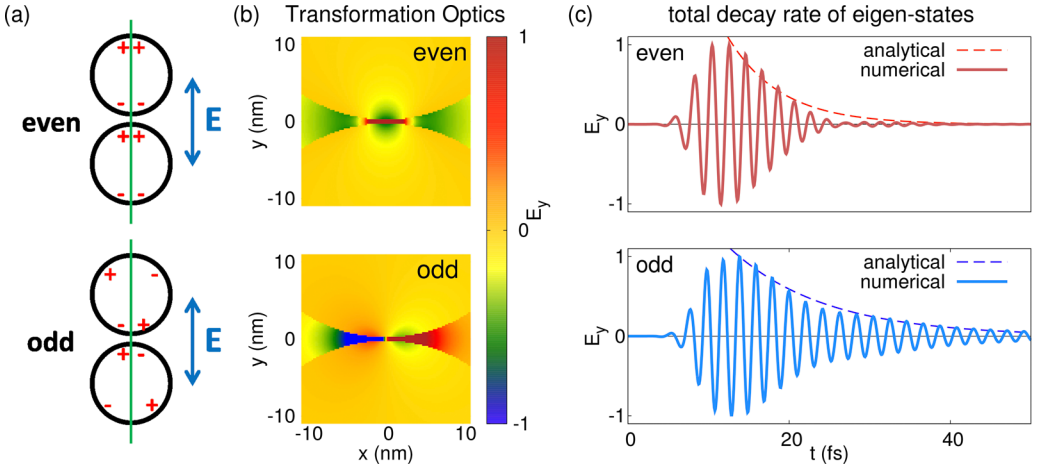

Figure 2. (a) Plasmonic modes supported by a dimer structure for an E_y-polarized plane-wave excitation. The even eigenstate is the only bright mode, while the odd eigenstate (and all antibonding states, not shown) are dark. (b) Field profile and enhancement predicted from the transformation optics analytical description. (c) Decay of the even and odd bonding eigenstates calculated numerically and analytically using eq 1.

to a progressively larger phase difference between the central and peripheral antinodes. Due to the weaker excitation of the quadrupole mode, its peripheral lobes dissipate before the dipole mode.

At ∼27 fs the dipole mode has decayed significantly and mode beating characteristics appear, with a mode that has a node at $x \approx 0$. Once the dipole mode has completely decayed, the node settles at $x = 0$ and the field has opposite phase at each side of the x-axis. These field characteristics are distinctively different from the dipole mode and are in fact due to the odd-bonding mode of the plasmonic dimer structure, which exhibits orthonormal features to the even-bonding mode and decays slower.[34] In Figure 2, we show the supported first-order ($n = 1$) bonding eigenstates of the dimer structure over the y-axis mirror symmetry (i.e., determined by the E_y-polarization excitation) of the dimer structure[2,34] (see Figure S2 for all bonding and antibonding modes supported by the dimer structure). External radiation (from the even continuum) primarily couples to the even-bonding eigenstates that by definition are bright, and the first ($n = 1$ and second-order ($n = 2$) even eigenstates correspond to the dipole and quadrupole modes shown in Figure 1c. However, the odd-bonding modes are also excited (although less efficiently) and appear on the spatiotemporal map once the even modes have radiated away most of their energy. The first order odd-bonding mode is excited with external illumination due to the extremely small gap and leads to the mode beating features seen in Figure 1e with the even and eigenstate. Due to reciprocity, the odd-bonding state radiates inefficiently to the even continuum and is therefore a dark mode with a slower decay rate than the even mode.

Using a transformation optics analytical description (Supporting Information, Section 1), we obtain the complex resonant frequencies for the nanowire dimer structure:

$$\omega_n^{\text{even}} = \sqrt{\frac{R_2^n - R_1^n}{2R_2^n}}\,\omega_p - i\left(\frac{\gamma_m}{2} + \frac{n\pi g^4 \omega_p^3}{8R_0^2 c_0^2}\left(\frac{R_1}{R_2}\right)^n \sqrt{\frac{R_2^n - R_1^n}{2R_2^n}}\right)$$

$$\omega_n^{\text{odd}} = \sqrt{\frac{R_2^n - R_1^n}{2R_2^n}}\,\omega_p - i\frac{\gamma_m}{2} \qquad (1)$$

where n denotes the nth-order mode, R_1, R_2, and R_0 are geometrical constants in the transformed space, and γ_m and ω_p are the damping and plasma frequency of a Drude metal. The real part of the two eigenstates reveals that both even and odd eigenstates for the nanowire dimer are always resonant at the same frequency, but have different imaginary parts. The $\gamma_m/2$ term describes the ohmic dissipation of each mode, and the additional imaginary term of ω_n^{even} describes its radiative decay to the far field. Hence, the even eigenstates are bright (radiate to the continuum) and odd eigenstates are dark, and the transformation optics analytical description predicts their field profiles shown in Figure 2b. The different decay rates of the dipole ($n = 1$) even- and odd-bonding eigenstates are shown in Figure 2b, where we plot the normalized E_y field of the even and odd eigenstates, together with the predicted mode decay described by eq 1. One can see that the even eigenstate decays more rapidly than the odd mode, since it radiates efficiently to the far field, and this behavior is predicted very well by eq 1. The analytical description also describes well the decay rate of higher-order modes (see Supporting Information, Section 2, Figure S3).

The odd eigenstates are commonly neglected when considering plasmonic gaps.[34] It is usually assumed that due to their dark nature, external illumination does not couple to them efficiently. While this assumption is valid for larger gaps (i.e., > 5 nm) where the intrinsic odd mode of each nanoparticle is strongly confined on each nanoparticle, for extremely small gaps of just 1−2 nm they hybridize with each other and manage to confine their field enhancement in the gap. Hence, for plasmonic nanocavities with extreme gaps, there is an additional contribution to the field enhancement, due to the excitation of the odd-bonding modes, leading to spatial asymmetries in the spatiotemporal map of Figure 1e.

To study the strong-coupling spatiotemporal dynamics in this system, we surround the two nanowires with a homogeneous layer of QEs, which we model with the semiclassical Maxwell−Bloch description for a two-level system shown in Figure 1d (see Methods for derivation), with characteristics $\omega_{12} = 3.033 \times 10^{15}$ (rad/s) ≈ 2 eV ⇒ $\lambda_{12} \approx 621$ nm, the excited state lifetime $\tau_{12} = 10^{-9}$ s, dephasing $\gamma_p = 6.457 \times 10^{13}$ Hz, and dipole moment $\mu = (4.11 \times 10^{-11} e)$ m (e = elementary electronic charge). Figure 1b shows the absorption cross-section for both the passive and strongly coupled system, where the characteristic Rabi splitting is seen for the dipole (even-bonding) mode. Figure 1g and h show the spatiotemporal

DOI: 10.1021/acsphotonics.7b00437
ACS Photonics 2017, 4, 2410−2418

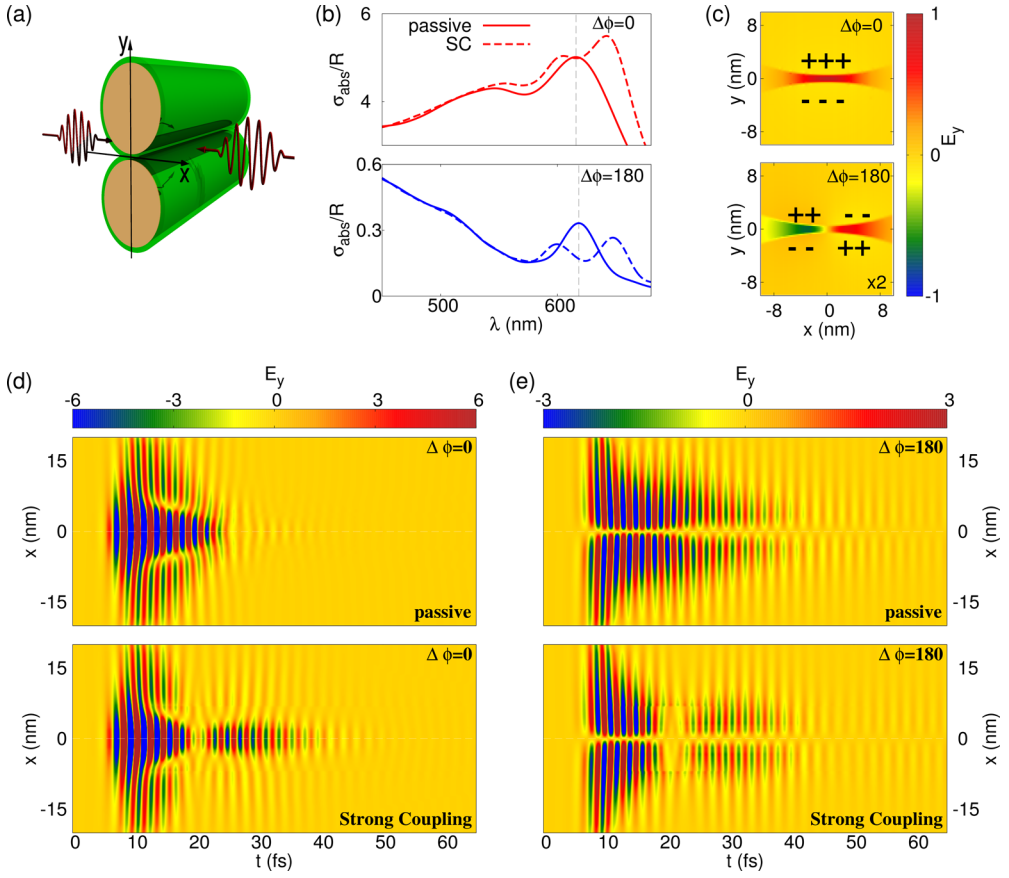

Figure 3. (a) Nanowire gold dimer structure with double-sided pulse excitation and a homogeneous layer of QEs shown in green. The absorption cross-section for (b) symmetric ($\Delta\phi = 0°$) and antisymmetric ($\Delta\phi = 180°$) excitation for the passive (full lines) and strongly coupled (dashed line) system. (c) Field profile of the first symmetric ($\Delta\phi = 0°$) and antisymmetric ($\Delta\phi = 180°$) modes, both occurring at $\lambda = 621$ nm. (d) Spatiotemporal dynamics of the passive (top) and strongly coupled (bottom) system for symmetric and (e) antisymmetric double-sided excitations.

map of the strongly coupled system. Initially, the incident broad-band pulse excites directly both the dipole and quadrupole modes, showing similar features to those for the passive system. But when the QE layer is present, at ∼18 fs, energy is absorbed from the plasmonic modes and re-emission emerges after ∼20 fs. This is the first energy exchange cycle and therefore the first lobe of the Rabi oscillations and is spatially asymmetric. At longer times (∼55 fs), mode beating features emerge within the Rabi oscillations, indicating that both the even- and odd-bonding eigenstates are simultaneously strongly coupled to the QE layer. In fact the odd eigenstate continues to exchange energy with the QEs for much longer than the even eigenstate. Hence, the strong coupling spatiotemporal dynamics are governed by a multiple set of modes all exchanging energy with QEs, but with different time dynamics.

Preserving Parity Symmetry. Due to the single-sided excitation of the above system, the y-axis symmetry of the dimer structure breaks, since the excited fields at $x > 0$ do not match the excited fields at $x < 0$. To obtain a better understanding on the individual coupling and energy exchange dynamics of the QEs with the even and odd modes alone, we tailor the external illumination to preserve the parity symmetry of the system (i.e., $\mathbf{E}(y) = \mathbf{E}(-y)$). To achieve this, we illuminate the structure with two identical sources, one propagating toward the $-x$-axis and the other toward the $+x$-axis (double-sided excitation, Figure 3a). By modulating the phase difference ($\Delta\phi$) of the two sources, one can excite the pure parity states of the system. For symmetric ($\Delta\phi = 0°$) illumination, only the even eigenstates are excited, and for antisymmetric ($\Delta\phi = 180°$) illumination only the odd eigenstates are excited, with the absorption cross-sections and mode profiles shown in Figure 3b and c, respectively. As eq 1 predicts, the symmetric and antisymmetric absorption spectra are resonant at similar wavelengths. Also the mode profiles of the even and odd eigenstates are in agreement with the even and odd eigensolutions of the transformation optics analytical model shown in Figure 2b. The antisymmetric ($\Delta\phi = 180°$) absorption cross-section is 1 order of magnitude smaller than the symmetric ($\Delta\phi = 06°$) one, since odd eigenstates are darker states. However, it is significant to note that the odd mode field enhancement is of the same order of magnitude as the even mode (Figure 3b), since the extremely small gap also confines the odd modes in the cavity, and therefore both eigenstates comparably contribute to the QE excitation.

The even and odd spatiotemporal maps for the passive dimer structure are shown in Figure 3d and e, respectively, and are distinctively different from each other. For the symmetric illumination ($\Delta\phi = 0°$), $n = 1$ and $n = 2$ even-bonding modes are excited, with the initial dynamics being almost identical to the single-sided excitation. However, different from Figure 1g, no spatial asymmetries or mode beating is present as the fields decay ($t > 30$ fs). The antisymmetric ($\Delta\phi = 180°$) spatiotemporal map in Figure 3e has a node at $x = 0$ nm, and the E_y-field has opposite phase at each side of the center, as predicted by the transformation optics analytical model. Also, the decay rate of the odd eigenstates is significantly slower than

DOI: 10.1021/acsphotonics.7b00437
ACS Photonics 2017, 4, 2410−2418

that of the even one and also in very good agreement with the transformation optics analytical description of eq 1. It should be noted that the single-sided spatiotemporal map of Figure 1e is the exact superposition of the symmetric and antisymmetric maps of Figure 3d and e.

We now place a homogeneous layer of QEs around the nanowire dimer structure, represented by a two-level semiclassical Maxwell−-Bloch description (Methods). The absorption cross-sections for the symmetric ($\Delta\phi$ = 0°) and antisymmetric ($\Delta\phi$ = 180°) double-sided excitations are shown in Figure 3b, and both show the characteristic Rabi splitting for the absorption spectra and therefore are both strongly coupled to the QE layer. The two spatiotemporal maps of the two strongly coupled systems are shown in Figure 3d and e (bottom figures). They reveal the Rabi oscillations induced due to the QE coupling with each of the eigenstates separately. To directly observe the energy induced in the plasmonic nanocavity directly from the QEs and therefore the Rabi dynamics, we plot in Figure 4a the macroscopic polarization P_{12} induced from the two-level system (see eq 6) for the single- and the two double-sided illuminations. The envelope of P_{12} corresponds to the Rabi oscillations and directly leads to the induced E-field re-emission seen in Figure 3d and e (see Supporting Information Section 4 for more discussion). In Figure 4b, we plot P_{12} for all three illumination types for comparison. Note that P_{12} for single excitation is irregularly shaped due to the spatial asymmetry of the energy exchange with QEs. The amplitude and time dynamics of the single-sided Rabi oscillations are again a superposition of each eigenstate's constituent strongly coupled dynamics (noting that $P_{12}^{\Delta\phi=180}$ has opposite phase than $P_{12}^{\Delta\phi=0}$).

Since we excite the system with a broadband pulse of duration ∼14 fs, by the time the first Rabi oscillation appears at ∼30 fs the direct plasmon excitation has decayed. Therefore, the Rabi oscillations shown in Figure 4b are the evolution of the energy exchange dynamics between the emitter and the plasmons *without* any external excitation. This is in contrast to steady-state calculations, where the steady-state plasmon oscillation continuously excites the QEs. The rapid decay of the Rabi oscillations is due to the very dissipative nature of plasmons. Each Rabi cycle couples less energy back to the QEs, since the plasmons dissipate the energy in ohmic losses. We demonstrate in the following section that despite the "bad" cavity and the different dissipation rates of the two eigenstate Rabi oscillations, the system is in the strong coupling regime with a coupling strength of $g \approx 75.6$ meV for both eigenstates.

DISCUSSION

A homogeneous layer of QEs placed in plasmonic nanocavities is strongly coupled to two sets of eigenstates (even and odd), which for the plasmonic nanowire dimer are spectrally degenerate. To obtain the coupling interaction of such a system, we derive a semiclassical analytical model describing the QE layer as a homogeneous two-level system coupled simultaneously to two photonic modes (see Methods). The hybrid states are obtained from the solution of the eigenvalue problem:

$$[(\omega - \Omega_{QE})(\omega - \Omega_1) - KA_{11}][(\omega - \Omega_{QE})(\omega - \Omega_2) - KA_{22}] - K^2A_{12}A_{21} = 0 \quad (2)$$

where $\Omega_{QE} = \omega_{12} - i\gamma_{12}$ is the complex frequency of the two-level electronic transition with ω_{12} being the transition resonance frequency and $\gamma_{12} = \gamma_p$ the dephasing term; $\Omega_n = \omega_n - i\gamma_n$ is the complex frequency of a cavity mode with ω_n and γ_n being the frequency and line-width of the n eigenstate, $K = \frac{(N_1 - N_2)\,|\mu|^2}{3\hbar\varepsilon_0\varepsilon_d} \approx \frac{N_d\,|\mu|^2}{3\hbar\varepsilon_0\varepsilon_d}$, N_1 and N_2 are the occupation densities of the ground and excited states, respectively, N_d is the total carrier density, μ is the dipole moment of the electronic transition, ε_d is the permittivity of the background material, and A_{nn}, A_{nk} are coupling coefficients (where n, k refer to the plasmonic eigenstates). A_{nn} denotes the coupling of mode n with the QE layer alone, and A_{nk} the coupling of mode k with mode n via the QEs. Equation 2 shows that each cavity mode independently couples to QEs (A_{nn}), but mode n can also couple to mode k via the QEs (A_{nk}) described by the last term of eq 2.

To initially obtain the direct coupling (A_{nn}) of the two eigenstates, we detune the resonance frequency (ω_{QE}) of the QE layer and calculate the absorption spectrum for the symmetric and antisymmetric double-sided excitations using FDTD. Although it is not feasible to "tune" ω_{QE} experimentally, it is appropriate for the theoretical study presented here in order to leave the two plasmon modes $\Omega_{1,2}$ of eq 2 undisturbed. To obtain the detuning maps experimentally, one would need to vary the plasmon frequencies $\Omega_{1,2}$ by changing either the radius of the nanowires or the gap between them. However, this would change both the frequency and line-width of the two plasmon modes, as well as the field enhancement in the gap from each mode, and therefore add further complexity to the detuning maps. The detuning maps are plotted in Figure 5a and b for the even and odd eigenstates, respectively, and reveal the characteristic anticrossing of the hybrid states, with the size of the white dots representing the value of the absorption cross-section peak calculated numerically. Since for double-sided illumination only one eigenstate is excited, and the superposition of the symmetric and antisymmetric spatiotemporal maps leads to the spatiotemporal map of the single excitation, we can

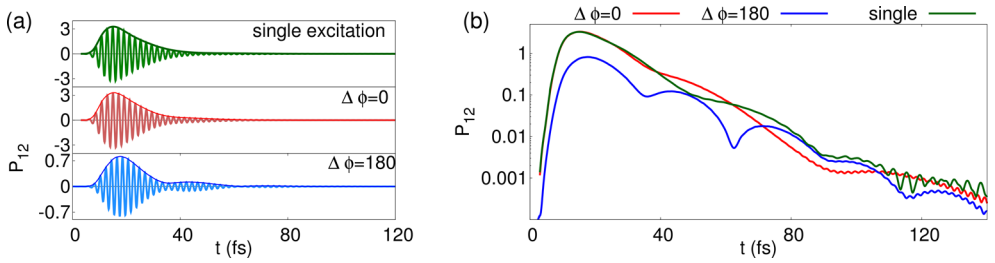

Figure 4. (a) P_{12} at x = 3.2 nm for single excitation (green) and symmetric (red) and antisymmetric (blue) excitations, with the indicated envelope revealing the Rabi oscillations. (b) Rabi oscillations for the symmetric (red) and antisymmetric (blue) double-sided and single-sided (green) excitations at x = 3.2 nm.

DOI: 10.1021/acsphotonics.7b00437
ACS Photonics 2017, 4, 2410−2418

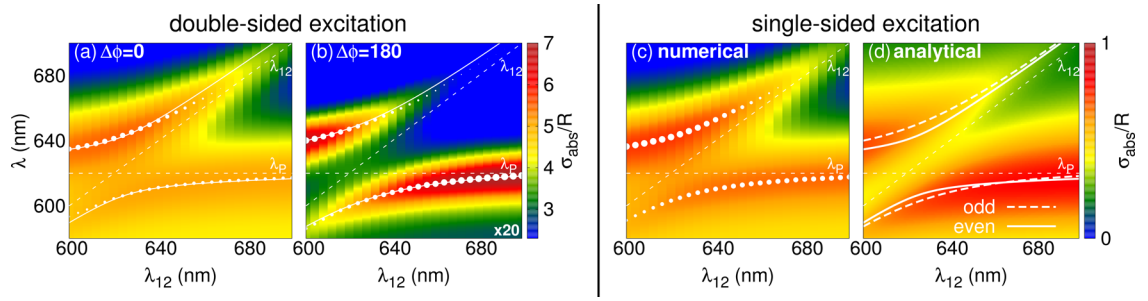

Figure 5. Detuning maps for (a) symmetric and (b) antisymmetric double-sided excitation and (c) single-sided excitation. We detune $\omega_{12} = 2\pi c/\lambda_{12}$ of the two-level QEs from the plasmon frequency (which remains undisturbed). The size of the white dots represents the value of σ_{abs}, and white lines are the analytical model fit to extract the coupling strength. (d) Analytical calculations for σ_{abs} using a semiclassical model when both the even and odd eigenstates are strongly coupled to QEs.

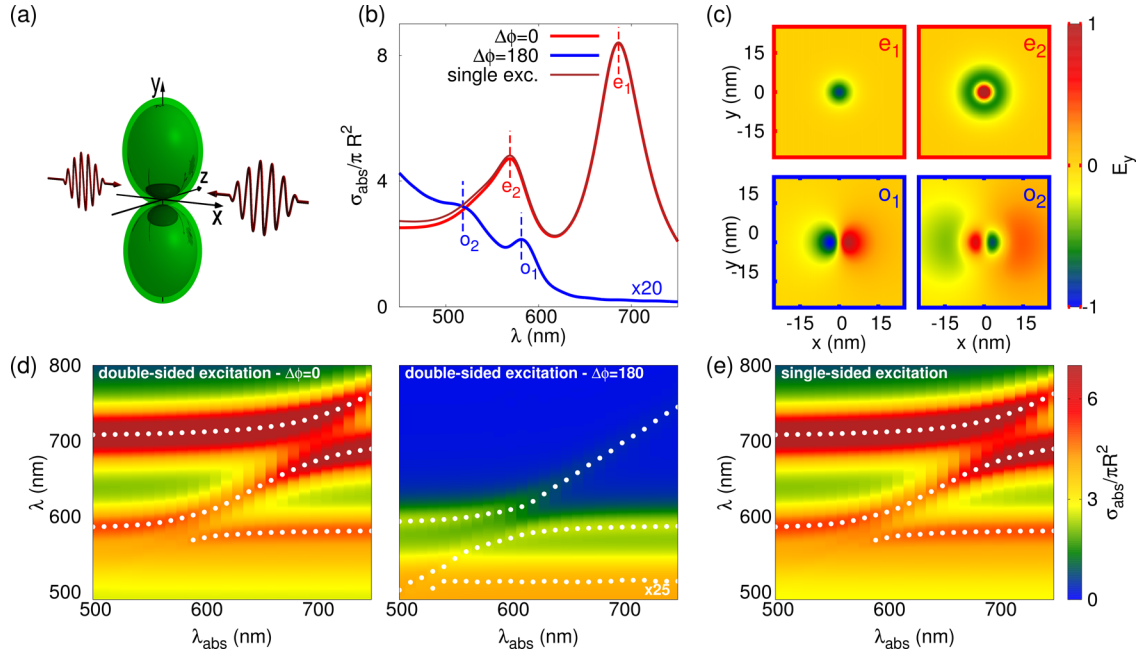

Figure 6. (a) 3D spherical nanoparticle dimer struture. (b) Absorption cross-section σ_{abs} for the symmetric (red) and antisymmetric (blue) double-sided excitation. The labels e_1 and e_2 refer to the first- and second-order even bonding eigenstates and o_1 and o_2 to the odd eigenstates. (c) Field profiles of the first- and second-order even and odd eigenstates. (d) Detuning maps for the symmetric (left figure) and antisymmetric (right figure) double-sided excitation. (e) Detuning map for single-sided excitation. We detune $\omega_{12} = 2\pi c/\lambda_{12}$ of the two-level QEs from the plasmon frequency (which remains undisturbed).

conclude that $K^2 A_{12} A_{21} \Rightarrow 0$, and therefore there is no significant cross-coupling between the two eigenstates. Hence, the eigenvalue problem of eq 2 is reduced to the single-mode coupled system:[38]

$$\omega_{\pm}^{\text{even,odd}} = \frac{1}{2}(\Omega_{\text{QE}} + \Omega_{e,o}) \pm \frac{1}{2}\sqrt{(\Omega_{\text{QE}} - \Omega_{e,o})^2 + 4KA_{ee,oo}} \quad (3)$$

where $\omega_{\pm}^{\text{even}}$ and $\omega_{\pm}^{\text{odd}}$ are the hybrid states of the even and odd plasmonic eigenstates and the effective coupling strength is given by $g_{ee,oo} = \sqrt{KA_{ee,oo}}$. We plot eq 3 with lines in Figure 5a and b, using the complex frequencies of the two eigenstates and QEs, and fit it to the numerical data to obtain the coupling strengths of the two modes: $g_{ee} = g_{oo} = \sqrt{KA_{ee,oo}} = 75.6$ meV. With the complex frequencies of the two eigenstates determined from the numerical simulations ($\omega_e = \omega_0 = 2\pi c_0/621$ nm ≈ 2 eV and $Q_e = 7.16$ and $Q_o \approx 19.5$, giving $\Omega_{e,o} = \omega_{e,o} - i\omega_{e,o}/2Q_{e,o}$), the only fit parameters that enter eq 3 are the overlap factors $U_{nk} = \langle u_n, u_k \rangle_g$ (see Methods, eq 7), which in turn enter A_{nk} and consequently determine the values of g_{ee} and g_{oo}. For these calculations, we assumed that $U_{nn} = U_{kk} = 0.5$ (i.e., half the field energy is in the QE layer) and neglect cross-coupling between the even and odd eigenstates, $U_{nk} = U_{kn} = 0$.

Despite the different nature of the even and odd eigenstates, their different field enhancement (odd field enhancement is half of the even mode), mode profile, and Q-factors, they surprisingly have identical effective coupling strengths. To get better insight for this surprising result, we note that $g \propto \sqrt{\frac{n}{V}}$, where n is the number of emitters coupled to each mode and V is the mode volume, which is a measure of the each mode's spatial confinement and for our 2D nanowire structure reduces to "mode area". For the nanowire plasmonic structure discussed in this paper, the "mode area" of the even eigenstate is ~4 nm^2 and the odd eigenstate ~5.6 nm^2. This means that the odd

DOI: 10.1021/acsphotonics.7b00437
ACS Photonics 2017, 4, 2410−2418

mode energy is less confined in the gap than for the even mode and therefore is strongly coupled to more emitters (i.e., n is also larger), which makes the two coupling strengths equal. Additionally, the Purcell factor is $F_P \propto \left(\frac{Q}{V}\right)$ and takes values $F_P^e \approx 1.8$ and $F_P^o \approx 3.5$ for the even and odd modes. This is due to the nonradiative nature of the odd eigenstate, which compensates for its smaller field enhancement since more Rabi cycles can be facilitated.

Using the effective coupling strength value of the two modes ($g_{ee} = g_{oo} = 75.6$ meV) and eq 3, we find the complex Rabi frequency for the even, $\Omega_R^e = (9.14 - i5.25) \times 10^{13}$ (rad/s) $\Rightarrow$ $\omega_R^e \approx 60$ meV, and the odd mode, $\Omega_R^o = (17.34 - i0.137) \times 10^{13}$ (rad/s) $\Rightarrow$ $\omega_R^o \approx 114$ meV. Taking into account only the real part of these values, we find the two Rabi time periods $\tau_R^e = 68.77$ fs and $\tau_R^o = 36.24$ fs for the even and odd modes, respectively. This is in good agreement with our numerical results shown in Figure 4b, where $\tau_R^e = 60$ fs and $\tau_R^o = 27$ fs. In Figure 5c and d, we show the detuning map for a single-sided excitation obtained numerically and analytically using the semiclassical model. Since $\omega_{even} = \omega_{odd}$ and $g_{ee} = g_{oo}$, the two sets of hybrid states overlap in frequency (Figure 5d). Then we can safely conclude that for single-sided excitation where two plasmonic modes are excited, QEs simultaneously, but independently, exchange energy with both the even and odd eigenstates.

Rotationally Symmetric Structures. So far, we have been discussing the cavity modes of a nanowire dimer (2D structure), which is *mirror* symmetric over the y-axis. To extend the above concepts to 3D symmetries, we consider two spherical nanoparticles forming a dimer (see Figure 6a), which is *rotationally* symmetric with respect to the y-axis. Now, the spherical harmonics of the electrostatic potential do not collapse to $e^{im\phi}$, as for the 2D dimer, and the even and odd eigenstates are therefore spectrally separated. The absorption cross-sections for the symmetric and antisymmetric double-sided excitations of the 3D dimer are shown in Figure 6b together with the single illumination spectra, which show the even and odd modes being spectrally separated as expected. One can see that the o_1 mode is resonant at higher frequencies than e_1 and in fact spectrally closer to e_2. The field profiles of the first- and second-order even (e_1, e_2) and odd (o_1, o_2) bonding modes are also shown in Figure 6c. In general, the odd eigenstates are less radiative for rotational than for mirror symmetric structures.

The detuning maps (detuning of ω_{12} of QEs) for the 3D dimer structure (Figure 6d) show a clear anticrossing for the e_1 mode and the e_2 mode. o_1 and o_2 modes show anticrossings for the antisymmetric detuning map, but do not significantly contribute to the single-sided detuning map (Figure 6e) because the odd eigenstates radiate too inefficiently to be recorded in the far field. The spatiotemporal map of the 3D dimer (see Supporting Information, Figure S3) shows that e_1 is dominantly excited with the single-sided excitation pulse, with no mode beatings observed. Although the odd eigenstates are still excited and are coupled to the QEs, the Rabi oscillations of the e_1 eigenstate are dominant.

Other structures with mirror and rotational symmetry are the nanowire and nanoparticle on mirror (NWoM and NPoM) configurations. Their even and odd eigenstates and their strong coupling spatiotemporal dynamics (see Supporting Information, Figure S3) show the corresponding behavior to their parity symmetry. Hence, in our earlier work where we experimentally reported[27] the strong coupling of a single molecule in NPoM (which is rotationally symmetric), the molecule is coupled to the first-order even mode (e_1) alone, and the dark modes forming the "pseudomode"[39] do not contribute toward the Rabi dynamics of the strongly coupled system, contrary to earlier reports.[39]

Plasmonic nanostructures have been shown to be a versatile environment to realize strong coupling at room temperature.[19,25,27] In this work, we demonstrate that plasmonic nanocavities exhibit different types of plasmons depending on the nanostructure's parity symmetry. They can be selectively excited by tailoring the external illumination to exploit the parity symmetry of the nanoplasmonic structure. A homogeneous layer of emitters placed in a plasmonic nanocavity can therefore be driven simultaneously by two types of modes (bright and dark), which leads to complex Rabi dynamics for the hybrid system. We demonstrate that the coupling strength of the QE layer with two such types of modes is identical, regardless of their different nature, field enhancement, and profile. In conclusion, the parity symmetry of plasmonic nanocavities is of great importance in the strong coupling regime, since it determines the spatiotemporal coupling dynamics with the enclosing QE medium and can be potentially used to control and tailor dynamically the Rabi-cycle dynamics of a plasmon−exciton hybrid system.

METHODS

Maxwell−Bloch Description of QEs. The two-level QEs are described using the Maxwell−Bloch equations with density matrix elements given by[40] (see Supporting Information, Section 3 for derivation)

$$\begin{aligned} \partial_t \rho_{12} &= -(\Gamma - i\omega_{12})\rho_{12} - i\frac{\boldsymbol{\mu}\cdot\mathbf{E}}{\hbar}(\rho_{22} - \rho_{11}) \\ \partial_t \rho_{22} &= -\partial_t \rho_{11} = -\gamma\rho_{22} - \frac{2\boldsymbol{\mu}\cdot\mathbf{E}}{\hbar}\mathrm{Im}(\rho_{12}) \end{aligned} \tag{4}$$

where $\Gamma = 6.457 \times 10^{13}$ Hz, $\gamma = 1/\tau_{21} = 1/10^{-9}$ (s^{-1}) is the relaxation rate of the excited state, $\boldsymbol{\mu} = 4.11 \times 10^{-11}$ e m, $\hat{\mathbf{u}}_y$ is the dipole moment of the electronic transition (e = elementary electronic charge), $\mathbf{E}$ is the local E-field at the position of a QE, and $\omega_{12} = 3.033 \times 10^{15}$ (rad/s) ≈ 2 eV is the transition frequency of the two-level QEs. The above equations lead to the population evolution of the two energy states as

$$\frac{\partial N_2}{\partial t} = -\frac{\partial N_1}{\partial t} = -\gamma N_2 + \frac{1}{\hbar\omega_{12}}\left(\frac{\partial \mathbf{P}}{\partial t} + \Gamma\mathbf{P}\right)\cdot\mathbf{E} \tag{5}$$

where N_1 and N_2 are the carrier densities at the ground and excited state, respectively.

Since the macroscopic polarization response from the two-level system is given by $\mathbf{P} = N_d\,\boldsymbol{\mu}\rho_{12}$, where N_d is the total carrier density, the macroscopic polarization due to the excitation of the two-level system is

$$\frac{\partial^2 \mathbf{P}}{\partial t^2} + 2\Gamma\frac{\partial \mathbf{P}}{\partial t} + (\Gamma^2 + \omega_{12}^2)\mathbf{P} = -\frac{2\omega_{12}|\mu|^2}{\hbar}(N_2 - N_1)\mathbf{E} \tag{6}$$

Semiclassical Analytical Model. The $\mathbf{E}$ of eq 6 represents the local electromagnetic classical fields from the plasmonic structure, which is a superposition of (damped) electromagnetic modes with complex frequency $\Omega_n = \omega_n - i\gamma_n$. Considering the normal modes $\mathbf{u}_n(\mathbf{r})$, then $\mathbf{E}_n(\mathbf{r}, t) = \mathbf{u}_n(\mathbf{r})\hat{E}_n(t)\ e^{-i\Omega_n t}$.

DOI: 10.1021/acsphotonics.7b00437
ACS Photonics 2017, 4, 2410−2418

Inserting this in Maxwell's equations and considering a slowly varying envelope approximation gives

$$\partial_t E_n(t) = -\mathrm{i}\Omega_n E_n(t) + \mathrm{i}\frac{\omega^2}{2\Omega_n}\langle \mathbf{u}_n^*(\mathbf{r})\cdot\mathbf{u}_{\mathrm{inc}}\rangle F_{\mathrm{inc}}(t) + \mathrm{i}\sum_k A_{nk}P_k(t)/\varepsilon_0 \tag{7}$$

where $A_{nk} = \frac{\omega_k^2}{2\omega_n\varepsilon_{r,g}}\langle \mathbf{u}_n^*(\mathbf{r})\cdot\mathbf{u}_k(\mathbf{r})\rangle_{\mathrm{QE}} = \frac{\omega_k^2}{2\omega_n\varepsilon(\mathbf{r})}U_{nk}$ describes the coupling of modes n and k, U_{nk} is an overlap term between the two modes, F_{inc} is the driving term given by $F_{\mathrm{inc}}(t) = E_{\mathrm{inc}}(t) + \frac{\langle \mathbf{u}_n^*(\mathbf{r})\cdot\mathbf{u}_{\mathrm{inc}}\rangle_{\mathrm{QE}}}{\langle \mathbf{u}_n^*(\mathbf{r})\cdot\mathbf{u}_{\mathrm{inc}}\rangle_{\varepsilon_{r,\mathrm{QE}}\varepsilon_0}}P_{\mathrm{inc}}(t)$, and $P_k(t)$ is the polarization of the two-level system coupled to mode k. Combining eq 7 for the two electromagnetic modes with eq 6 for the induced polarizations of the two-level system yields the eigenvalue problem of the coupled system:

$$\begin{pmatrix} \Omega_{\mathrm{QE}}-\omega & 0 & -K & 0 \\ 0 & \Omega_{\mathrm{QE}}-\omega & 0 & -K \\ -A_{11} & -A_{12} & \Omega_1-\omega & 0 \\ -A_{21} & -A_{22} & 0 & \Omega_2-\omega \end{pmatrix}\begin{pmatrix} P_1/\varepsilon_0 \\ P_2/\varepsilon_0 \\ E_1 \\ E_2 \end{pmatrix} = 0 \tag{8}$$

where $K = \frac{|\mu|^2}{\hbar\varepsilon_0}(N_1 - N_2)$, $\Omega_{\mathrm{QE}} = \omega_{\mathrm{QE}} - \mathrm{i}\Gamma_{\mathrm{QE}}$ with ω_{QE} and Γ_{QE} are the transition resonance frequency and total dephasing rate of the two-level system, and Ω_1 and Ω_2 are the complex resonant frequencies of the plasmonic modes given by $\Omega_{1,2} = \omega_{1,2} - \mathrm{i}\gamma_{1,2}$. Hence the eigenvalues emerge as

$$[(\omega-\Omega_{\mathrm{QE}})(\omega-\Omega_1) - KA_{11}][(\omega-\Omega_{\mathrm{QE}})(\omega-\Omega_2) - KA_{22}] - K^2A_{12}A_{21} = 0 \tag{9}$$

For a system where there is no cross-coupling between the two modes via the QEs (i.e., $A_{12} = A_{21} = 0$), the dispersion of the hybrid states simplifies to

$$\omega_{\pm}^{1,2} = \frac{1}{2}(\Omega_{\mathrm{QE}} + \Omega_{1,2}) \pm \frac{1}{2}\sqrt{(\Omega_{\mathrm{QE}} - \Omega_{1,2})^2 + 4KA_{11,22}} \tag{10}$$

with the effective coupling strength $g_{\mathrm{eff}}^{11,22} = \sqrt{KA_{11,22}}$, and therefore the two modes split without "feeling" each other. The coupling factor $K \approx 8.31 \times 10^{12}$ $(\mathrm{ms^2\ A})^{-1}$ is a constant since our system is in the small signal regime (i.e., $N_1 - N_2 = N_d = 10^{27}$ $\mathrm{m^{-3}}$ and $\mu/e = 4 \times 10^{-11}$ m), $\omega_{\mathrm{even,odd}} = 3.011 \times 10^{15}$ $\mathrm{s^{-1}}$ are obtained from the absorption spectra in Figure 3a and b, and $\gamma_{\mathrm{even}} = 2.1 \times 10^{14}$ s^{-1} and $\gamma_{\mathrm{odd}} = 7.73 \times 10^{13}$ $\mathrm{s^{-1}}$ from quality factor calculations for the plasmonic nanocavity ($Q_{\mathrm{even,odd}} = \omega_{\mathrm{even,odd}}/2\gamma_{\mathrm{even,odd}}$).

On the other hand, if $A_{12} \neq 0$ and $A_{21} \neq 0$ (which is not the case for the systems described in this article) and the coupling strength to the two modes is the same (i.e., $A_{11} = A_{22}$), with $\Omega_1 = \Omega_2$, then the hybrid states of the strongly coupled system are given by

$$\omega_{\pm,\pm} = \frac{1}{2}(\Omega_{\mathrm{QE}} + \Omega_1) \pm \frac{1}{2}\sqrt{(\Omega_{\mathrm{QE}} - \Omega_1)^2 + 4K(A_{11} \pm \sqrt{A_{12}A_{21}})} \tag{11}$$

Absorption Energy. The total energy absorbed per time, $W_{\mathrm{abs}} = \partial u/\partial t$, of the incident field is

$$W_{\mathrm{abs}} = \sum_l \varepsilon_0\overline{\langle \varepsilon^{(b)}\dot{\mathbf{E}}_l\cdot\mathbf{E}_{\mathrm{inc}}\rangle} + \sum_l \overline{\langle \dot{\mathbf{P}}_l\cdot\mathbf{E}_{\mathrm{inc}}\rangle} + \overline{\langle \dot{\mathbf{P}}_{\mathrm{inc}}\cdot\mathbf{E}_{\mathrm{inc}}\rangle} \tag{12}$$

where the bar indicates temporal averaging and the bracket spatial averaging. The terms account for the work exercised by the incident field directly on the plasmonic modes (first term) and on the polarized QE medium (second and third term). For time-harmonic excitation, we thus obtain

$$W_{\mathrm{abs}} = \sum_l \frac{\omega}{2}\varepsilon_0\langle \varepsilon^{(b)}\mathrm{Im}[\mathbf{E}_l^*\cdot\mathbf{E}_{\mathrm{inc}}]\rangle + \sum_l \frac{\omega}{2}\langle \mathrm{Im}[\mathbf{P}_l^*\cdot\mathbf{E}_{\mathrm{inc}}]\rangle + \sum_l \frac{\omega}{2}\langle \mathrm{Im}[\mathbf{P}_{\mathrm{inc}}^*\cdot\mathbf{E}_{\mathrm{inc}}]\rangle \tag{13}$$

and using the aforementioned definitions for the overlap factors and effective background permittivity we obtain

$$W_{\mathrm{abs}} = \sum_l \frac{\omega}{2}\varepsilon_0\varepsilon_{l,\mathrm{inc}}^{(b)}\mathrm{Im}[E_l^*\cdot E_{\mathrm{inc}}] + \sum_l \frac{\omega}{2}\Gamma_{l,\mathrm{inc}}^{(g)}\mathrm{Im}[P_l^*\cdot E_{\mathrm{inc}}] + \sum_l \frac{\omega}{2}\Gamma_{\mathrm{inc,inc}}^{(g)}\mathrm{Im}[P_{\mathrm{inc}}^*\cdot E_{\mathrm{inc}}] \tag{14}$$

■ ASSOCIATED CONTENT

Supporting Information

The Supporting Information is available free of charge on the ACS Publications website at DOI: 10.1021/acsphotonics.7b00437.

Full derivation for the transformation optics analytical model, classification of the supported eigenstates for the nanowire dimer system and decay rates of each eigenstate, derivation of the semiclassical Maxwell−Bloch description, further discussion on the Rabi oscillations, and further data showing that our results depend on the parity symmetry of the nanoplasmonic structure (PDF)

■ AUTHOR INFORMATION

Corresponding Authors

*E-mail: a.demetriadou06@imperial.ac.uk.
*E-mail: o.hess@imperial.ac.uk.

ORCID

Angela Demetriadou: 0000-0001-7240-597X
Yu Luo: 0000-0003-2925-682X
Jeremy J. Baumberg: 0000-0002-9606-9488
Ortwin Hess: 0000-0002-6024-0677

Notes

The authors declare no competing financial interest.

■ ACKNOWLEDGMENTS

We acknowledge financial support from EPSRC grants EP/L027151/1, EU LINASS 320503, and EP/L024926/1 and the Royal Society International Exchanges grant IE151097. J.B. Pendry acknowledges support from the Gordon and Betty Moore foundation.

■ REFERENCES

(1) Aubry, A.; Lei, D. Y.; Fernandez-Dominguez, A. I.; Sonnefraud, Y.; Maier, S. A.; Pendry, J. B. Plasmonic Light-Harvesting Devices over the Whole Visible Spectrum. *Nano Lett.* **2010**, *10*, 2574−2579.

DOI: 10.1021/acsphotonics.7b00437
ACS Photonics 2017, 4, 2410−2418

(2) Giannini, V.; Fernandez-Dominguez, A. I.; Heck, S. C.; Maier, S. A. Plasmonic Nanoantennas: Fundamentals and Their Use in Controlling the Radiative Properties of Nanoemitters. *Chem. Rev.* **2011**, *111*, 3888−3912.
(3) Mirkin, C. A.; Letsinger, R. L.; Mucic, R. C.; Storhoff, J. J. A DNA-based method for rationally assembling nanoparticles into macroscopic materials. *Nature* **1996**, *382*, 607.
(4) Stewart, M. E.; Anderton, C. R.; Thompson, L. B.; Maria, J.; Gray, S. K.; Rogers, J. A.; Nuzzo, R. G. Nanostructured Plasmonic Sensors. *Chem. Rev.* **2008**, *108*, 494−521.
(5) Anker, J. N.; Hall, W. P.; Lyandres, O.; Shah, N. C.; Zhao, J.; Duyne, R. P. V. Biosensing with plasmonic nanosensors. *Nat. Mater.* **2008**, *7*, 442−453.
(6) Kneipp, K.; Wang, Y.; Kneipp, H.; Perelman, L. T.; Itzkan, I.; Dasari, R. R.; Feld, M. S. Single Molecule Detection Using Surface-Enhanced Raman Scattering (SERS). *Phys. Rev. Lett.* **1997**, *78*, 1667.
(7) Ma, R.-M.; Oulton, R. F.; Sorger, V. J.; Bartal, G.; Zhang, X. Room-temperature sub-diffraction-limited plasmon laser by total internal reflection. *Nat. Mater.* **2011**, *10*, 110−113.
(8) Anger, P.; Bharadwaj, P.; Novotny, L. Enhancement and Quenching of Single-Molecule Fluorescence. *Phys. Rev. Lett.* **2006**, *96*, 113002.
(9) Mertens, H.; Koenderink, A. F.; Polman, A. Plasmon-enhanced luminescence near noble-metal nanospheres: Comparison of exact theory and an improved Gersten and Nitzan model. *Phys. Rev. B: Condens. Matter Mater. Phys.* **2007**, *76*, 115123.
(10) Raizen, M.; Thompson, R.; Brecha, R.; Kimble, H.; Carmichael, H. Normal-Mode Splitting and Linewidth Averaging for Two-State Atoms in an Optical Cavity. *Phys. Rev. Lett.* **1989**, *63*, 240−243.
(11) Zhu, Y.; Gauthier, D. J.; Morin, S.; Wu, Q.; Carmichael, H.; Mossberg, T. Vacuum Rabi Splitting as a Feature of Linear-Dispersion Theory: Analysis and Experimental Observations. *Phys. Rev. Lett.* **1990**, *64*, 2499−2502.
(12) Rempe, G.; Thompson, R.; Brecha, R.; Lee, W.; Kimble, H. Optical Bistability and Photon Statistics in Cavity Quantum Electrodynamics. *Phys. Rev. Lett.* **1991**, *67*, 1727−1730.
(13) Thompson, R.; Rempe, G.; Kimble, H. Observation of Normal-Mode Splitting for an Atom in an Optical Cavity. *Phys. Rev. Lett.* **1992**, *68*, 1132−1135.
(14) Yoshie, T.; Scherer, A.; Hendrickson, J.; Khitrova, G.; Gibbs, H. M.; Rupper, G.; Ell, C.; Shchekin, O. B.; Deppe, D. G. Vacuum Rabi splitting with a single quantum dot in a photonic crystal nanocavity. *Nature* **2004**, *432*, 200−203.
(15) Faraon, A.; Fushman, I.; Englund, D.; Stoltz, N.; Petroff, P.; Vuckovic, J. Coherent generation of non-classical light on a chip via photon-induced tunnelling and blockade. *Nat. Phys.* **2008**, *4*, 859−863.
(16) Groblacher, S.; Paterek, T.; Kaltenbaek, R.; Brukner, S. C.; Dotukowski, M. Z.; Aspelmeyer, M.; Zeilinger, A. An experimental test of non-local realism. *Nature* **2007**, *446*, 871−875.
(17) Reithmaier, J. P.; Sek, G.; Loffler, A.; Hofmann, C.; Kuhn, S.; Reitzenstein, S.; Keldysh, L. V.; Kulakovskii, V. D.; Reinecke, T. L.; Forchel, A. Strong coupling in a single quantum dot-semiconductor microcavity system. *Nature* **2004**, *432*, 197−200.
(18) Schlather, A. E.; Large, N.; Urban, A. S.; Nordlander, P.; Halas, N. J. Near-Field Mediated Plexcitonic Coupling and Giant Rabi Splitting in Individual Metallic Dimers. *Nano Lett.* **2013**, *13*, 3281−3286.
(19) Delga, A.; Feist, J.; Bravo-Abad, J.; Garcia-Vidal, F. Quantum Emitters Near a Metal Nanoparticle: Strong Coupling and Quenching. *Phys. Rev. Lett.* **2014**, *112*, 253601.
(20) Delga, A.; Feist, J.; Bravo-Abad, J.; Garcia-Vidal, F. Theory of strong coupling between quantum emitters and localized surface plasmons. *J. Opt.* **2014**, *16*, 114018.
(21) Gonzalez-Ballestero, C.; Feist, J.; Moreno, E.; Garcia-Vidal, F. J. Harvesting excitons through plasmonic strong coupling. *Phys. Rev. B: Condens. Matter Mater. Phys.* **2015**, *92*, 121402.
(22) Vakevainen, A.; Moerland, R.; Rekola, H.; Eskelinen, A.; Martikainen, J.; Kim, D.; Torma, P. Plasmonic Surface Lattice Resonances at the Strong Coupling Regime. *Nano Lett.* **2014**, *14*, 1721−1727.
(23) Eizner, E.; Avayu, O.; Ditcovski, R.; Ellenbogen, T. Aluminum Nanoantenna Complexes for Strong Coupling between Excitons and Localized Surface Plasmons. *Nano Lett.* **2015**, *15*, 6215−6221.
(24) Wang, H.; Wang, H.-Y.; Bozzola, A.; Toma, A.; Panaro, S.; Raja, W.; Alabastri, A.; Wang, L.; Chen, Q.-D.; Xu, H.-L.; Angelis, F. D.; Sun, H.-B.; Zaccaria, R. P. Dynamics of Strong Coupling between J-Aggregates and Surface Plasmon Polaritons in Subwavelength Hole Arrays. *Adv. Funct. Mater.* **2016**, *26*, 6198−6205.
(25) Zengin, G.; Wersall, M.; Nilsson, S.; Antosiewicz, T. J.; Kall, M.; Shegai, T. Realizing Strong Light-Matter Interactions between Single-Nanoparticle Plasmons and Molecular Excitons at Ambient Conditions. *Phys. Rev. Lett.* **2015**, *114*, 157401.
(26) Wersall, M.; Cuadra, J.; Antosiewicz, T. J.; Balci, S.; Shegai, T. Observation of Mode Splitting in Photoluminescence of Individual Plasmonic Nanoparticles Strongly Coupled to Molecular Excitons. *Nano Lett.* **2017**, *17*, 551−558.
(27) Chikkaraddy, R.; de Nijs, B.; Benz, F.; Barrow, S. J.; Scherman, O. A.; Rosta, E.; Demetriadou, A.; Fox, P.; Hess, O.; Baumberg, J. J. Single-molecule strong coupling at room temperature in plasmonic nanocavities. *Nature* **2016**, *535*, 127.
(28) Zhang, Y.; Meng, Q.-S.; Zhang, L.; Luo, Y.; Yu, Y.-J.; Yang, B.; Zhang, Y.; Esteban, R.; Aizpurua, J.; Luo, Y.; Yang, J.-L.; Dong, Z.-C.; Hou, J. G. Sub-nanometre control of the coherent interaction between a single molecule and a plasmonic nanocavity. *Nat. Commun.* **2017**, *8*, 15225.
(29) Mubeen, S.; Zhang, S.; Kim, N.; Lee, S.; Kramer, S.; Xu, H.; Moskovits, M. Plasmonic Properties of Gold Nanoparticles Separated from a Gold Mirror by an Ultrathin Oxide. *Nano Lett.* **2012**, *12*, 2088−2094.
(30) Mertens, J.; Eiden, A. L.; Sigle, D. O.; Huang, F.; Lombardo, A.; Sun, Z.; Sundaram, R. S.; Colli, A.; Tserkezis, C.; Aizpurua, J.; Milana, S.; Ferrari, A. C.; Baumberg, J. J. Controlling Subnanometer Gaps in Plasmonic Dimers Using Graphene. *Nano Lett.* **2013**, *13*, 5033−5038.
(31) Mertens, J.; Demetriadou, A.; Bowman, R.; Benz, F.; Kleemann, M.; Tserkezis, C.; Shi, Y.; Yang, H.; Hess, O.; Aizpurua, J.; Baumberg, J. Tracking optical welding through groove modes in plasmonic nanocavities. *Nano Lett.* **2016**, *16*, 5605−5611.
(32) Monroe, C. Quantum information processing with atoms and photons. *Nature* **2002**, *416*, 238−246.
(33) Shalabney, A.; George, J.; Hutchison, J.; Pupillo, G.; Genet, C.; Ebbesen, T. W. Coherent coupling of molecular resonators with a microcavity mode. *Nat. Commun.* **2015**, *6*, 5981.
(34) Halas, N. J.; Lal, S.; Chang, W.-S.; Link, S.; Nordlander, P. Plasmons in Strongly Coupled Metallic Nanostructures. *Chem. Rev.* **2011**, *111*, 3913−3961.
(35) Sun, G.; Khurgin, J. Comparative study of field enhancement between isolated and coupled metal nanoparticle: An analytical approach. *Appl. Phys. Lett.* **2010**, *97*, 263110.
(36) Sun, G.; Khurgin, J. Theory of optical emission enhancement by coupled metal nanoparticles: An analytical approach. *Appl. Phys. Lett.* **2011**, *98*, 113116.
(37) Kongsuwan, N.; Demetriadou, A.; Chikkaraddy, R.; Benz, F.; Turek, V. A.; Keyser, U. F.; Baumberg, J. J.; Hess, O. Suppressed Quenching of Purcell-Enhanced Single-Molecule Emission in Plasmonic Nanocavities. *arXiv:1612.02611*, 2016.
(38) Torma, P.; Barnes, W. L. Strong coupling between surface plasmon polaritons and emitters: a review. *Rep. Prog. Phys.* **2015**, *78*, 013901.
(39) Li, R.-Q.; Hernangomez-Perez, D.; Garcia-Vidal, F.; Fernandez-Dominguez, A. Transformation Optics Approach to Plasmon-Exciton Strong Coupling in Nanocavities. *Phys. Rev. Lett.* **2016**, *117*, 107401.
(40) Boyd, R. W. *Non-linear Optics*, 3rd ed.; Academic Press: London, 2008.

DOI: 10.1021/acsphotonics.7b00437
ACS Photonics 2017, 4, 2410−2418